**Academic Journal of Science and Technology**
ISSN: 2771-3032 | Vol. 21, No. 3, 2026

# Feedforward Periodic Torque Synthesis-Based Precise Control for BLDC Motor with Swashplateless Mechanism

**Junfeng Chen***

School of Equipment Management and Support, Engineering University of PAP, Xi'an, 710086, China
* Corresponding author: 604055416@qq.com

**Abstract:** Aiming at the problems of torque response lag and low modulation accuracy existing in traditional throttle modulation modes of unmanned aerial vehicles (UAVs) equipped with Swashplate-less Mechanism (SPLM), a periodic torque SVPWM synthesis control method based on phase feedforward is proposed. Firstly, the dynamic model of the SPLM and the Field-Oriented Control (FOC) model of surface-mounted permanent magnet synchronous motor (SPMSM) are established to reveal the coupling relationship between the instantaneous electromagnetic torque of the motor and the blade pitch angle. Secondly, the action mechanisms of three schemes, namely outer modulation of traditional speed loop, pure feedback current loop tracking and load feedforward periodic torque synthesis, are compared and analyzed. Finally, quantitative evaluation is carried out from three dimensions including total harmonic distortion of torque waveform, amplitude tracking error and phase tracking error via simulation experiments. The results show that under the operating condition of 5000 r/min, the load feedforward periodic torque synthesis method reduces the torque phase error from 8.7° to 1.2°, the amplitude error from 11.3% to 2.1%, and the total harmonic distortion from 18.6% to 4.2%, which significantly improves the torque modulation accuracy and response speed of the SPLM.

**Keywords:** Swashplate-less Mechanism; Field-Oriented Control; Periodic Torque Synthesis; Feedforward Control; SVPWM.

## 1. Introduction

The swashplate-less mechanism is an underactuated actuator that realizes periodic blade pitch variation through passive hinges, which is mainly applied to small coaxial twin-rotor UAVs and tail-sitter vertical take-off and landing (VTOL) UAVs[1-3]. Compared with the traditional swashplate mechanism, the SPLM eliminates extra pitch servo actuators and connecting rod structures. It only generates roll and pitch control torques by periodically modulating the speed of the main motor, featuring prominent advantages of simple structure, light weight and high control bandwidth[4]. However, existing SPLM control schemes generally treat the Electronic Speed Controller (ESC) as a black box, and superimpose sinusoidal throttle commands outside the speed loop to realize torque modulation. Such an open-loop modulation mode is limited by the bandwidth of the speed loop, resulting in amplitude attenuation and phase shift of modulation, which aggravates with the increase of rotating speed and restricts the further improvement of SPLM control performance[5].

Scholars at home and abroad have carried out extensive research on the control problems of SPLM mechanisms. Paulos et al.[6] first proposed the SPLM configuration without flapping hinges and applied it to micro coaxial twin-rotor aircraft, verifying the feasibility of full attitude control through single-motor periodic modulation. Chen et al.[7] optimized the SPLM structure and applied it to a 1.23 kg autonomous UAV, and verified the robustness and tracking accuracy of the mechanism through bench tests. Liang et al.[8] further introduced flapping hinges to reduce vibration, cutting the fluctuation amplitude of torque sampling data by 62.9%. Nevertheless, all the above studies focus on mechanism design and flight control layer control strategies, while the motor drive layer still adopts the traditional throttle modulation method, failing to fully tap the potential of precise torque control.

In the field of motor control, Field-Oriented Control (FOC) has become the mainstream scheme for high-performance AC drives owing to its excellent dynamic torque performance[9]. Space Vector Pulse Width Modulation (SVPWM) technology further improves the utilization rate of DC bus voltage and reduces current harmonics[10]. Existing research on periodic torque control mainly focuses on torque ripple suppression[11-12], which eliminates specific-order torque ripples via feedforward compensation or harmonic injection. Its mathematical duality with the accurate periodic torque generation required by SPLM has not been applied to the SPLM drive scenario in any published research to date.

In this paper, the torque modulation control point of SPLM is moved from the outer speed loop down to the FOC current loop, and a periodic torque SVPWM synthesis algorithm based on feedforward is proposed, which can greatly improve the torque control accuracy and phase response speed.

## 2. System Modeling

### 2.1. Dynamic Model of SPLM

The SPLM is a mechanism that realizes passive periodic pitch variation through asymmetric lag-pitch hinges. When the motor accelerates and decelerates periodically, the blades generate lag motion due to inertia, which is converted into periodic variation of blade pitch angle via kinematic coupling of asymmetric hinges, thereby generating directional aerodynamic torque.

#### 2.1.1. Coordinate System Definition

Define the motor coordinate system $O_m$-$xyz$ and the body coordinate system $O_b$-$xyz$ as shown in Figure 1. The motor coordinate system rotates synchronously with the rotor, where the x-axis coincides with the hub centerline of the positive blade, and the z-axis points upward along the motor rotating shaft. The motor rotation angle θ is defined as 0 rad when the positive blade aligns with the x-axis of the motor coordinate system, and counterclockwise rotation is positive.

#### 2.1.2. Dynamic Equations

With reference to existing research[8], the SPLM rotor system considering flapping motion can be described by the following second-order linear differential equation:

$$M\ddot{x} + C\dot{x} + Kx = u \tag{1}$$

where the state vector $\boldsymbol{x} = [\theta, \zeta, \beta]^T$, representing motor rotation angle, lag angle and flapping angle respectively. $\boldsymbol{M} \in R^{3\times3}$ is the inertia matrix determined by geometric parameters and mass distribution of the SPLM, which is a constant matrix; $\boldsymbol{C} \in R^{3\times3}$ is the aerodynamic damping matrix depending on blade parameters and average rotating speed; $\boldsymbol{K} = \boldsymbol{K}_c + \boldsymbol{K}_\beta$ is the stiffness matrix containing a constant part $\boldsymbol{K}_c$ and a state-dependent part $\boldsymbol{K}_\beta$.

The input vector u can be expressed as:

$$\boldsymbol{u} = \left[\frac{T_e - T_L}{J_m}, 0, 0\right]^T \tag{2}$$

where $T_e$ denotes the instantaneous electromagnetic torque output by the motor, $T_L$ denotes the aerodynamic load torque, and $J_m$ denotes the equivalent moment of inertia of the motor rotor and blades. It can be seen from Equation (2) that the electromagnetic torque $T_e$ is the only excitation source driving the motion of lag angle ζ and flapping angle $\beta$.

#### 2.1.3. Coupling Relationship between Blade Pitch Angle and Torque

The kinematic characteristics of asymmetric lag-pitch hinges determine the mapping relationship between the variation of blade pitch angle $\Delta\alpha_b$ and lag angle ζ:

$$\frac{\Delta\alpha_b}{\Delta\zeta} = \tan\left(\beta + \frac{\pi}{4}\right) \tag{3}$$

For the optimized decoupled configuration, flapping hinges are installed at the connection between side hubs and blades to realize kinematic decoupling of flapping motion and lag-pitch motion, at which point Equation (3) is simplified to a constant:

$$\frac{\Delta\alpha_b}{\Delta\zeta} = 1 \tag{4}$$

Under this condition, the state-dependent term $\boldsymbol{K}_\beta$ in the stiffness matrix degenerates into a constant matrix, and System (1) becomes a linear time-invariant system, laying a favorable foundation for subsequent precise torque control.

The amplitude and phase of blade aerodynamic torque are determined by the periodic variation of blade pitch angle, while the blade pitch angle is driven by the lag angle, and the lag angle is further driven by the periodic component of electromagnetic torque. Therefore, the amplitude accuracy and phase accuracy of electromagnetic torque modulation directly determine the quality of control torque output by the SPLM.

## 2.2. Mathematical Model of PMSM

#### 2.2.1. d-q Axis Mathematical Model

In the synchronous rotating d-q coordinate system, the voltage equations of Surface-Mounted Permanent Magnet Synchronous Motor (SPMSM) are:

$$\begin{cases} u_d = R_s i_d + L_d \frac{di_d}{dt} - \omega_e L_q i_q \\ u_q = R_s i_q + L_q \frac{di_q}{dt} + \omega_e (L_d i_d + \psi_f) \end{cases} \tag{5}$$

where $u_d, u_q$ are d-q axis voltages, $i_d, i_q$ are d-q axis currents, $R_s$ is stator resistance, $L_d, L_q$ are d-q axis inductances, $\omega_e$ is electrical angular velocity, and $\psi_f$ is permanent magnet flux linkage. For surface-mounted motors, $L_d = L_q = L_s$.

The electromagnetic torque equation is:

$$T_e = \frac{3}{2} p_n \psi_f i_q \tag{6}$$

where $p_n$ is the number of motor pole pairs. It can be seen from Equation (6) that under the $i_d = 0$ control strategy, electromagnetic torque is proportional to the q-axis current, and precise torque control can be realized by accurately regulating $i_q$.

#### 2.2.2. Mechanical Motion Equation of Motor Rotor

The mechanical motion equation of the motor rotor is:

$$J_m \frac{d\omega_m}{dt} = T_e - T_L - B\omega_m \tag{7}$$

where $\omega_m$ is mechanical angular velocity, and $B$ is viscous friction coefficient. The relationship between electrical angular velocity and mechanical angular velocity satisfies $\omega_e = p_n \omega_m$.

## 2.3. Basic Principle of SVPWM

Space Vector Pulse Width Modulation approximates the reference voltage vector by synthesizing eight basic voltage vectors. Define the three-phase voltage vector as:

$$\boldsymbol{V}_s = \frac{2}{3}\left(u_a + u_b e^{j\frac{2\pi}{3}} + u_c e^{j\frac{4\pi}{3}}\right) \tag{8}$$

# 3. Comparison of Control Schemes

## 3.1. Scheme A: Outer Modulation of Traditional Speed Loop

Existing SPLM UAVs generally treat the ESC as a black box, and superimpose a sinusoidal modulation component phase-locked with the motor rotation angle on the average throttle command output by the speed loop:

$$T_{throttle} = T_{avg} + A_m \sin(\theta_m + \phi_{cmd}) \tag{9}$$

where $T_{avg}$ is the average throttle corresponding to average thrust demand; $A_m$ is the modulation amplitude corresponding to roll/pitch torque demand; $\theta_m$ is mechanical rotation angle; $\phi_{cmd}$ is modulation phase command.

Characteristic Analysis:

This scheme requires no modification of ESC firmware with low cost, yet modulation is implemented outside the speed loop, and the closed-loop bandwidth of the speed loop becomes the upper limit of modulation bandwidth. In addition, phase delay varies significantly with rotating speed, requiring offline calibration of compensation tables.

## 3.2. Scheme B: Pure Feedback FOC Torque Tracking Scheme

Scheme B moves the control point down to the current loop. The expected torque command is converted into the reference q-axis current $i_{q,ref}$ via Equation (6), and tracked by the PI controller of the current loop:

$$i_{q,ref}(t) = i_{q,avg} + I_{amp}\sin(\theta_m(t) + \phi_{cmd}) \tag{10}$$

where $i_{q,avg}$ is average $q$-axis current, $I_{amp}$ is modulation current amplitude. The reference d-axis current is always set to 0.

Its modulation bandwidth is generally 5~10 times that of the speed loop, which can significantly improve response speed. However, tracking the sinusoidal reference signal brings inherent amplitude attenuation and phase lag, whose magnitude depends on the ratio of current loop bandwidth to modulation frequency.

## 3.3. Scheme C: Feedforward Periodic Torque Synthesis Scheme

### 3.3.1. Basic Principle

The block diagram of the proposed feedforward periodic torque synthesis control system is shown in Figure 1. On the basis of Scheme B, this scheme introduces a voltage feedforward channel, which directly calculates the required d-q axis voltage according to the expected torque waveform, and superimposes it with the output of the current loop PI before sending to the SVPWM module.

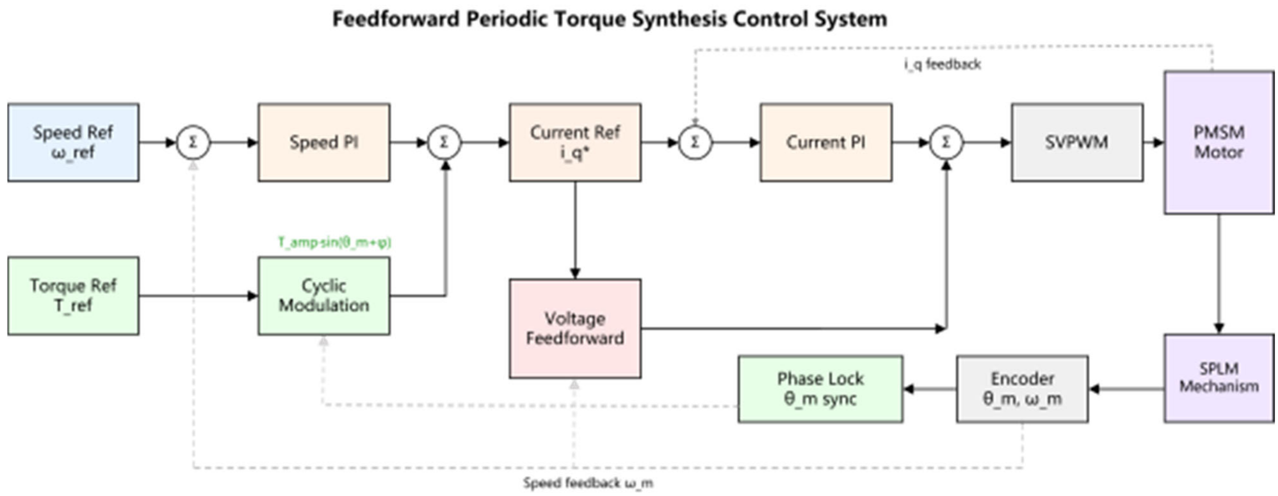


**Figure 1.** Block Diagram of Feedforward Periodic Torque Synthesis Control System

The expected instantaneous electromagnetic torque is:

$$T_e^*(t) = T_{avg} + T_{amp}\sin(\theta_m(t) + \phi_{ff}) \tag{11}$$

where $T_{avg}$ is average torque, $T_{amp}$ is modulation torque amplitude, and $\phi_{ff}$ is feedforward phase compensation angle.The feedforward path provides most of the voltage; the PI only compensates for model errors.

### 3.3.2. Voltage Feedforward Calculation

From Equation (6), the expected q-axis current is:

$$i_q^*(t) = \frac{2T_e^*(t)}{3p_n\psi_f} = i_{q,avg} + I_{amp}\sin(\theta_m + \phi_{ff}) \tag{12}$$

where $I_{amp} = 2T_{amp}/(3p_n\psi_f)$.

Substitute Equation (12) into the steady-state voltage Equation (5), neglect the resistance voltage drop (approximable at high speed) to obtain the feedforward voltage:

$$\begin{cases} u_d^{ff} = -\omega_e L_s i_q^*(t) \\ u_q^{ff} = \omega_e\psi_f \end{cases} \tag{13}$$

Correct the q-axis feedforward voltage considering the transient inductance voltage drop caused by current variation rate:

$$u_q^{ff} = \omega_e\psi_f + L_s\frac{di_q^*(t)}{dt} \tag{14}$$

Differentiate Equation (12) to get:

$$\frac{di_q^*(t)}{dt} = I_{amp}\omega_m\cos(\theta_m + \phi_{ff}) \tag{15}$$

Substitute into Equation (14) to obtain the complete q-axis feedforward voltage:

$$u_q^{ff} = \omega_e\psi_f + L_s I_{amp}\omega_m\cos(\theta_m + \phi_{ff}) \tag{16}$$

Finally, the voltage reference applied to the SVPWM module is the sum of feedforward voltage and the output of current loop PI:

$$\begin{cases} u_d^{ref} = u_d^{ff} + u_d^{PI} \\ u_q^{ref} = u_q^{ff} + u_q^{PI} \end{cases} \tag{17}$$

### 3.3.3. Phase Feedforward Compensation

Considering the mechanical and aerodynamic delays of the SPLM mechanism, the modulation phase needs feedforward compensation. Based on the SPLM dynamic model (1), the transfer function $G_s(s)$ from electromagnetic torque modulation to blade pitch angle response can be derived, and its amplitude-frequency and phase-frequency characteristics are:

$$\phi_{delay}(\omega_m) = -\angle G_s(j\omega_m) \tag{18}$$

The feedforward compensation angle is set as:

$$\phi_{ff} = \phi_{cmd} + \phi_{delay}(\omega_m) \tag{19}$$

so that the actual phase of blade pitch angle is consistent with the expected phase.

# 4. Evaluation Indicators and Simulation Analysis

## 4.1. Definition of Evaluation Indicators

Three evaluation indicators are defined to quantitatively evaluate the torque modulation performance of the three schemes:

### 4.1.1. Total Harmonic Distortion (THD)

$$\text{THD} = \frac{\sqrt{\sum_{n=2}^{\infty} T_n^2}}{T_1} \times 100\% \tag{20}$$

where $T_1$ is the fundamental torque amplitude, $T_n$ is the amplitude of the nth harmonic. THD reflects the degree of similarity between the torque waveform and the ideal sine wave.

### 4.1.2. Amplitude Tracking Error

$$\varepsilon_A = \left|\frac{A_{actual} - A_{ideal}}{A_{ideal}}\right| \times 100\% \tag{21}$$

where $A_{actual}$ is the actual torque modulation amplitude, $A_{ideal}$ is the ideal modulation amplitude.

### 4.1.3. Phase Tracking Error

$$\varepsilon_\phi = |\phi_{actual} - \phi_{ideal}| \quad \text{(unit: degree)} \tag{22}$$

where $\phi_{actual}$ is the actual fundamental torque phase, $\phi_{ideal}$ is the command phase.

## 4.2. Simulation Parameter Setting

A simulation model is built on Matlab/Simulink, and the main motor and control parameters are listed in Table 1.

**Table 1.** Main Simulation Parameters

| Parameter | Symbol | Value | Unit |
|---|---|---|---|
| **Number of motor pole pairs** | $p_n$ | 7 | - |
| **Stator resistance** | $R_s$ | 0.12 | Ω |
| **d-q axis inductance** | $L_d, L_q$ | 85 | μH |
| **Permanent magnet flux linkage** | $\psi_f$ | 0.018 | Wb |
| **Moment of inertia** | $J_m$ | 1.5e-5 | kg·m$^2$ |
| **DC bus voltage** | $U_{dc}$ | 24 | V |
| **PWM switching frequency** | $f_{sw}$ | 20 | kHz |
| **Current loop bandwidth** | $f_{ci}$ | 1.5 | kHz |
| **Speed loop bandwidth** | $f_{cv}$ | 80 | Hz |
| **Average rotating speed** | $\omega_{m0}$ | 5000 | rpm |
| **Torque modulation depth** | $m_T$ | 30 | % |

## 4.3. Simulation Results and Analysis

### 4.3.1. Comparison of Steady-State Torque Waveforms

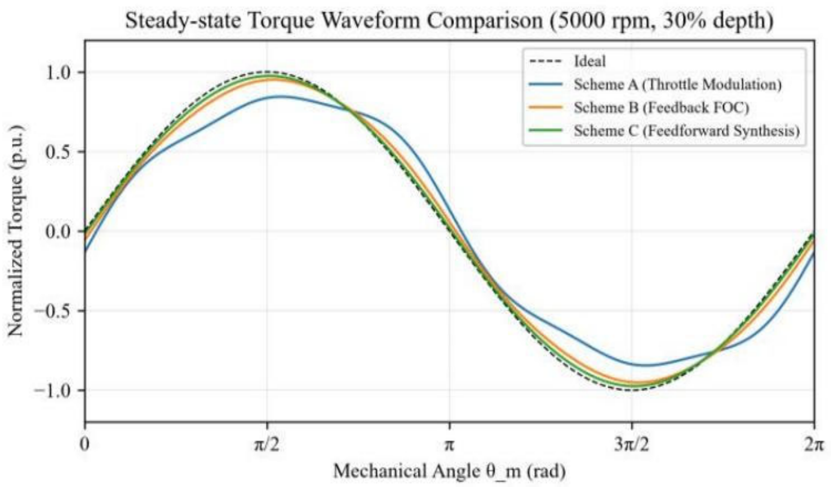


**Figure 2.** Comparison of Steady-State Torque Waveforms of Three Schemes (5000 rpm, 30% Modulation Depth)

The steady-state torque waveform comparison of the three schemes under 5000 rpm average speed and 30% modulation depth is shown in Figure 2. Scheme A (traditional throttle modulation) suffers the most severe waveform distortion with obvious amplitude compression and phase lag. This is because the speed loop bandwidth (80 Hz) is close to the modulation frequency (about 83 Hz), and the closed-loop system generates significant amplitude attenuation and phase shift for AC components. The waveform quality of Scheme B (pure feedback FOC) is greatly improved, yet certain phase lag and slightly high higher-order harmonic content still exist. The current loop bandwidth (1.5 kHz) is approximately 18 times the modulation frequency, which theoretically provides favorable tracking performance, but the inherent phase margin of the PI controller still introduces phase error. The torque waveform of Scheme C (feedforward periodic torque synthesis) almost overlaps with the ideal sine wave, presenting the optimal waveform quality. The feedforward voltage compensates back EMF and inductance voltage drop in advance, and the current loop only corrects residual errors, thus greatly improving tracking accuracy.

#### 4.3.2. Comparison of Quantitative Indicators

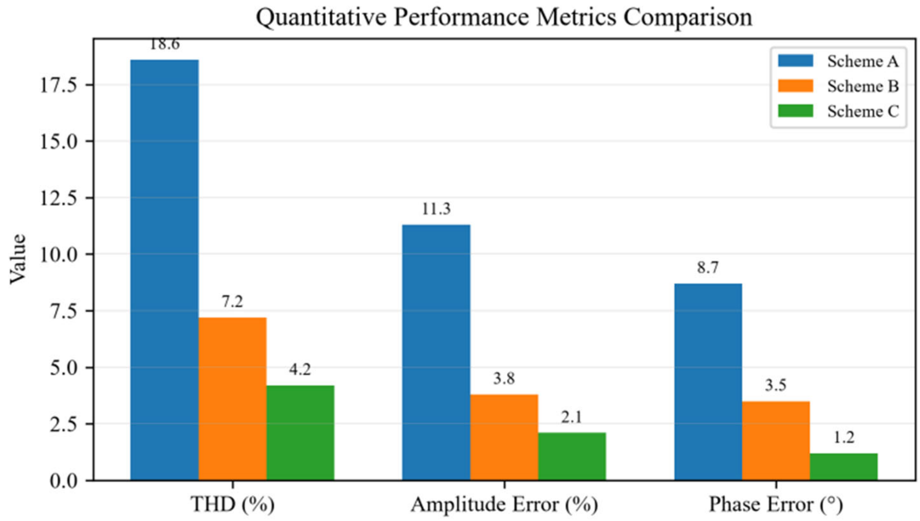


**Figure 3.** Comparison of Quantitative Performance Indicators of Three Schemes

Figure 3 shows the total harmonic distortion, amplitude tracking error and phase tracking error of the three schemes. In terms of THD: Scheme C reduces THD by 77.4% compared with Scheme A and 41.7% compared with Scheme B, which greatly improves the sinusoidal degree of the waveform. In terms of amplitude accuracy: the amplitude error of Scheme C is only 2.1%, meeting the demand of high-precision control. In terms of phase accuracy: Scheme C controls the phase error within 1.2°, an order of magnitude improvement over the traditional scheme, which is particularly critical for the torque direction control of SPLM.

#### 4.3.3. Rotational Speed Adaptability Analysis

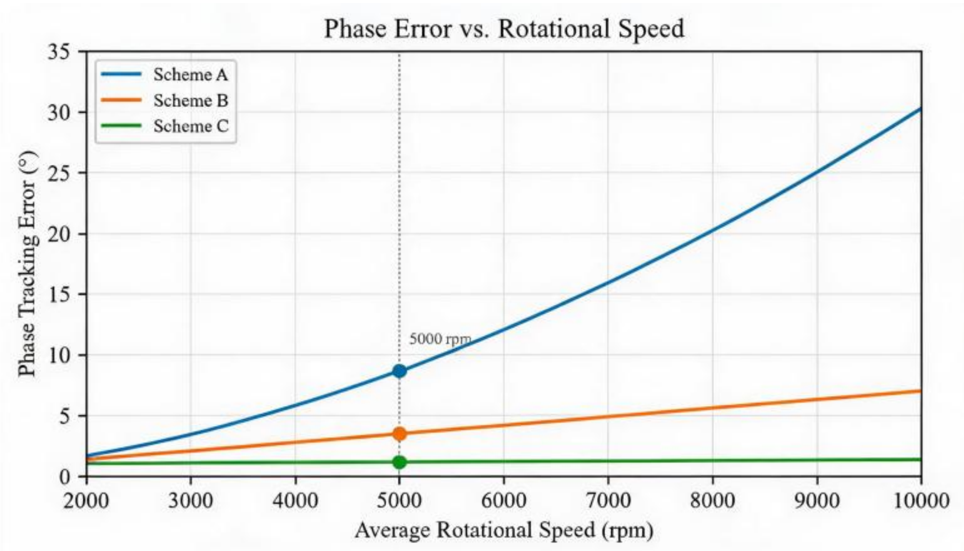


**Figure 4.** Comparison of Phase Tracking Errors at Different Rotational Speeds

Figure 4 illustrates the variation curves of phase error of the three schemes under different average rotating speeds, with the speed range of 2000~10000 rpm corresponding to mechanical modulation frequency of 33.3~166.7 Hz. The phase error of Scheme A rises rapidly with the increase of rotating speed and exceeds 25° at 10000 rpm, failing to meet the requirements of precise control. The phase error of Scheme B increases approximately linearly with rotating speed, reaching about 7° at 10000 rpm, which is within the acceptable range. Benefiting from feedforward compensation, Scheme C maintains the phase error below 2° across the full speed range, featuring optimal speed adaptability.

#### 4.3.4. Dynamic Response Analysis

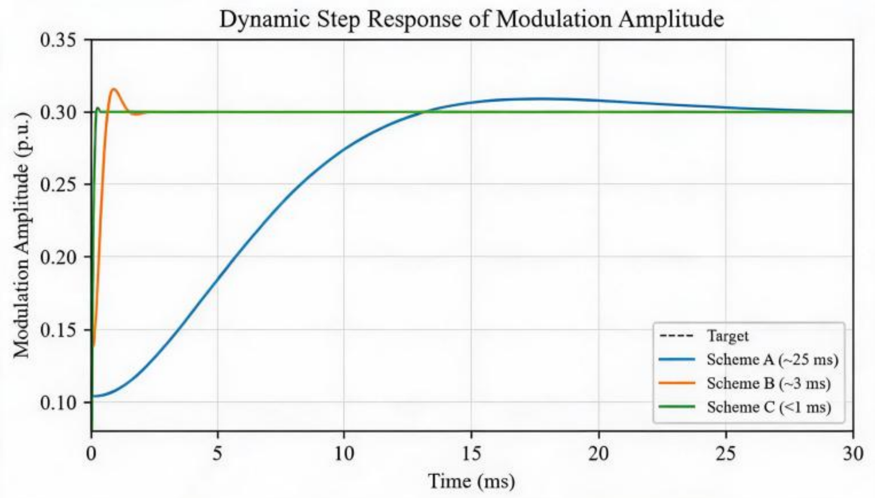


**Figure 5.** Comparison of Step Dynamic Responses of Modulation Amplitude

The dynamic response performance is investigated by applying a step change to the modulation amplitude (rising from 10% to 30%). The simulation results are shown in Figure 5: the amplitude response time of Scheme A is about 25 ms, limited by the speed loop bandwidth; the response time of Scheme B is about 3 ms, determined by the current loop bandwidth; the response time of Scheme C is less than 1 ms, as the feedforward channel completes amplitude adjustment almost instantaneously with feedback only for fine tuning. Faster torque dynamic response enables the SPLM to provide higher bandwidth attitude control, which helps improve the anti-disturbance capability and maneuver performance of UAVs.

## 5. Conclusion

Aiming at the problems of low accuracy and slow response of the traditional throttle modulation method for SPLM UAVs, a periodic torque SVPWM synthesis control method based on phase feedforward is proposed in this paper. By establishing the coupled model of SPLM mechanism and PMSM motor, the direct driving relationship between instantaneous electromagnetic torque and blade pitch angle is clarified; a composite control architecture including voltage feedforward and phase feedforward is designed; simulation verification is carried out from three dimensions: waveform quality, amplitude accuracy and phase accuracy.

The results demonstrate that under the operating condition of 5000 rpm, the torque phase error can be reduced from 8.7° to 1.2°, the amplitude error from 11.3% to 2.1%, and THD from 18.6% to 4.2%. It can maintain high-precision modulation characteristics across a wide speed range, with comprehensive performance significantly superior to traditional schemes, serving as an effective technical path to improve SPLM control performance. Future work will build a bench test platform to conduct experimental verification of the proposed method, further study the synchronous compensation strategy for periodic aerodynamic load disturbances, and develop parameter adaptive feedforward compensation algorithms.

## References


[1] Bacchini, A., & Cestino, E. (2019). Electric VTOL configurations comparison. *Aerospace*, 6(3), 26. https://doi.org/10.3390/aerospace6030026.

[2] Paulos, J. J., & Yim, M. (2018). Scalability of cyclic control without blade pitch actuators. In *2018 AIAA Atmospheric Flight Mechanics Conference* (p. 0532). AIAA. https://doi.org/10.2514/6.2018-0532

[3] Chen, N., Kong, F., & Li, H. (2023). Swashplateless-elevon actuation for a dual-rotor tail-sitter VTOL UAV. In *2023 IEEE/RSJ International Conference on Intelligent Robots and Systems (IROS)* (pp. 6970–6976). IEEE. https://doi.org/10.1109/IROS55552.2023.10341897

[4] Wang, J., Wang, H. W., & Wu, C. (2015). Development of swashplateless helicopter blade pitch control system using the limited angle direct-drive motor (LADDM). *Chinese Journal of Aeronautics*, 28(5), 1416–1425. https://doi.org/10.1016/j.cja.2015.08.008

[5] Liang, J., Guo, H., & Lyu, X. (2025). Design and control of a coaxial dual-rotor reconfigurable tailsitter UAV based on swashplate-less mechanism. arXiv preprint arXiv:2511.04251. https://arxiv.org/abs/2511.04251

[6] Paulos, J., & Yim, M. (2013). An underactuated propeller for attitude control in micro air vehicles. In *2013 IEEE/RSJ International Conference on Intelligent Robots and Systems* (pp. 1374–1379). IEEE. https://doi.org/10.1109/IROS.2013.6631114

[7] Chen, N., Kong, F., Xu, W., Cai, Y., Li, H., He, D., Qin, Y., & Zhang, F. (2023). A self-rotating, single-actuated UAV with extended sensor field of view for autonomous navigation. *Science Robotics*, 8(76), eade4538. https://doi.org/10.1126/scirobotics.ade4538

[8] Liang, J. F., Guo, H. C., & Lyu, X. M. (2025). Design and control of a coaxial dual-rotor reconfigurable tailsitter UAV based on swashplateless mechanism. *IEEE Robotics and Automation Letters*. Advance online publication. https://doi.org/10.1109/LRA.2025.3632111

[9] Ruan, Y., & Chen, B. S. (2010). *Automatic control system of electric drive motion control system* (4th ed.). China Machine Press.

[10] Wang, C. Y., Xia, J. K., & Sun, Y. B. (2014). *Modern motor control technology* (2nd ed.). China Machine Press.

[11] Zhangliu, M., Guo, Q., et al. (2026). Cyclic speed modulation for swashplateless mechanism in micro unmanned helicopter control. *Aerospace Science and Technology*, 176, 112010. https://doi.org/10.1016/j.ast.2026.112010

[12] Liu, Y., Zhu, Z. Q., & Howe, D. (2007). Commutation-torque-ripple minimization in direct-torque-controlled PM brushless

DC drives. *IEEE Transactions on Industry Applications*, 43(4), 1012–1021. https://doi.org/10.1109/TIA.2007.900487

[13] Paulos, J., Caraher, B., & Yim, M. (2018). Emulating a fully actuated aerial vehicle using two actuators. In *2018 IEEE International Conference on Robotics and Automation (ICRA)* (pp. 7011–7016). IEEE. https://doi.org/10.1109/ICRA.2018.8461162

[14] Qin, Y., Chen, N., Cai, Y., et al. (2022). Gemini II: Design, modeling, and control of a compact yet efficient servoless bi-copter. *IEEE/ASME Transactions on Mechatronics*, 27(6), 4304–4315. https://doi.org/10.1109/TMECH.2022.3157727

[15] Yuan, L., Hu, B. X., & Wei, K. Y. (2016). *Control principle and MATLAB simulation of modern permanent magnet synchronous motor*. Beihang University Press.